Spatially Distinct Tectonic Zones across Oklahoma Inferred from Shear-Wave Splitting

Angie D. Ortega-Romo[*1] , Jacob I. Walter[2] , Xiaowei Chen[1] , and Brett M. Carpenter[1]

Abstract

To better understand relationships among crustal anisotropy, fracture orientations, and the stress field in Oklahoma and southern Kansas, we conduct shear-wave splitting analysis on the last 9 yr of data (2010–2019) of local earthquake observations. Rather than a predominant fast direction (ϕ), we find that most stations have a primary fast direction of polarization (ϕ_{pri}) and a secondary fast direction of polarization (ϕ_{sec}). At most stations, either the primary fast direction of polarization (ϕ_{pri}) or the secondary fast direction of polarization (ϕ_{sec}) is consistent with the closest estimated maximum horizontal stress ($\sigma_{H\,max}$) orientation in the vicinity of the observation. The general agreement between fast directions of polarization (ϕ) and the maximum horizontal stress orientations ($\sigma_{H\,max}$) at the regional level implies that the fast polarization directions (ϕ) are extremely sensitive to the regional stress field. However, in some regions, such as the Fairview area in western Oklahoma, we observe discrepancies between fast polarization directions (ϕ) and maximum horizontal stress orientations ($\sigma_{H\,max}$), in which the fast directions are more consistent with local fault structures. Overall, the primary fast direction of polarization (ϕ_{pri}) is mostly controlled and influenced by the stress field, and the secondary fast direction of polarization (ϕ_{sec}) likely has some geologic structural control because the secondary direction is qualitatively parallel to some mapped north-striking fault zones. No significant changes in fast directions over time were detected with this technique over the 5 yr (2013–2018) of measurements, suggesting that pore pressure may not cause a significant enough or detectable change above the magnitude of the background stress field.

Introduction

The U.S. midcontinent, especially Oklahoma and southern Kansas, has experienced significant seismicity rate changes over the past decade, in which the number of seismic events dramatically increased from 2 to 3 **M** 3.0+ earthquakes per year in 2009 to ∼900 **M** 3.0+ earthquakes per year in 2015. Since then, the earthquake rate has slowly decreased, although seismicity is still significantly higher than pre-2009 historical rates (Schoenball and Ellsworth, 2017a; Walter *et al.*, 2020). These fluctuations in seismicity rates are linked to the significant amount of wastewater that was disposed of into the Arbuckle formation, which overlies the crystalline basement of the study region (Ellsworth, 2013; Walsh and Zoback, 2015; Schoenball and Ellsworth, 2017a). The crystalline basement rocks in Oklahoma and much of the U.S. midcontinent consist of Precambrian (∼1.4 Ga) Granite–Rhyolite craton (Denison *et al.*, 1984). This granitic basement hosts most of the seismicity of this region, where some earthquake sequences occur due to reactivation of pre-existing structures (Skoumal *et al.*, 2019).

However, most clusters of earthquakes occur on unmapped faults (Schoenball and Ellsworth, 2017a,b; Kolawole *et al.*, 2019) rather than those mapped within the Oklahoma Geological Survey (OGS) database (Marsh and Holland, 2016).

Holland (2013) and Darold *et al.* (2015) suggested an average maximum principal horizontal stress orientation of N85°E for southern Kansas and Oklahoma. Alt and Zoback (2017) estimated stress from waveform-derived focal mechanism solutions and wellbore measurements to produce a gridded regional stress field for broad areas of Oklahoma and southern Kansas. Qin *et al.* (2019) performed a more detailed stress inversion from a denser high-quality catalog of focal mechanisms from regional

1. School of Geosciences, The University of Oklahoma, Norman, Oklahoma, U.S.A., https://orcid.org/0000-0001-6188-4231 (ADOR); https://orcid.org/0000-0001-6362-3297 (XC); https://orcid.org/0000-0002-3451-2528 (BMC); 2. Oklahoma Geological Survey, The University of Oklahoma, Norman, Oklahoma, U.S.A., https://orcid.org/0000-0001-7127-9422 (JIW)

*Corresponding author: aortegaromo@ou.edu

and local earthquakes and provided a more detailed analysis of the local stress field for central Oklahoma and southern Kansas. Qin et al. (2019) also showed that most seismogenic faults (northeast- and northwest-trending) are optimally oriented with respect to the local stress field, except for certain distinct areas such as near Fairview, Oklahoma. The OGS fault database (Marsh and Holland, 2016) and the Qin et al. (2019) stress database provide a comprehensive understanding of the pre-existing fault and stress state of the midcontinent crust in Oklahoma and southern Kansas. We use these recent findings to support the shear-wave splitting (SWS) analysis described in this article and to better understand regional shear-wave polarization that may be caused by underlying geologic structures and/or regional stresses.

The splitting of shear waves occurs when a shear wave encounters an anisotropic medium and splits into two polarized quasishear waves (Crampin, 1984), with one wave arriving first with faster velocity and the second wave arriving later with slower velocity and typically orthogonal to the direction of the faster shear wave. The two SWS parameters that help quantify the anisotropy in the medium are delay time (δt) and fast polarization direction (ϕ). δt represents the difference in arrival time between the fast and slow shear waves, and it is proportional to the percentage of anisotropy in the medium. ϕ is the direction of fast polarization and may be influenced by the orientation of the structure that is causing the anisotropy in the area. The SWS technique has been used in myriad studies, mostly for monitoring relative crustal stress changes (Savage, Ohminato, et al., 2010; Unglert et al., 2011; Johnson and Savage, 2012) and to map fracture networks (Verdon et al., 2009; Gao et al., 2011; Wuestefeld et al., 2011; Baird et al., 2013).

Tadokoro and Ando (2002) performed an SWS analysis on the Nojima fault zone in Japan to study the healing process of the fault after earthquake rupture. About 9–12 months after rupture, ϕ was parallel to the fault strike. Subsequently, 33–45 months after earthquake rupture, ϕ rotated and was parallel to the regional maximum horizontal stress ($\sigma_{H\,max}$), suggesting that the fault has completely healed (Tadokoro and Ando, 2002). In addition, Li and Peng (2017) performed a systematic SWS analysis in southern California, in which ϕ is mainly controlled by regional stresses and some fault structures and is mainly consistent with $\sigma_{H\,max}$. In this study, we used an automatic SWS technique called the multiple filter automatic splitting technique (MFAST; Savage, Wessel, et al., 2010) to measure SWS parameters (ϕ and δt). We also consider whether those parameters vary temporally in Oklahoma and southern Kansas and compare with other datasets (e.g., Qin et al., 2019) to better understand the controlling factors of seismic anisotropy and its relationship with geological structures.

Data

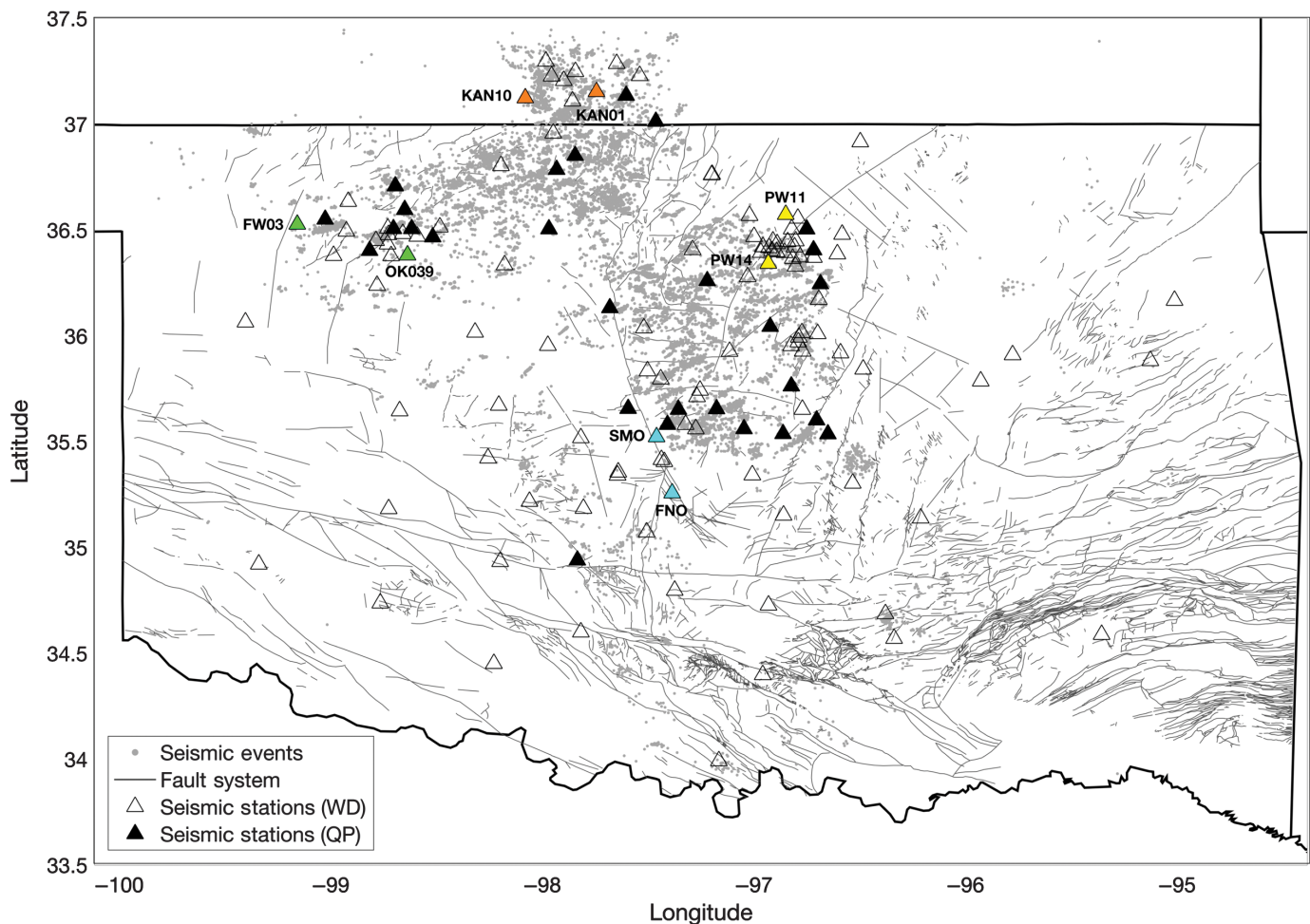We used the OGS earthquake catalog (Walter et al., 2020), including 33,367 events in Oklahoma from January 2010 to September 2019. The events range in magnitude from **M** 1.0 to **M** 5.8 and in depth from 0 to 45.25 km, with a median depth of 6.50 km. The seismicity map is displayed in Figure 1. The earthquakes were recorded by 148 seismic stations operated by the OGS including the Oklahoma Seismic Network (OK) and the Oklahoma Consolidated Temporary Seismic Network (O2) and other stations operated by other agencies, such as the U.S. Geological Survey Network (GS) and stations adjacent to the state of Oklahoma (see Data and Resources). Most of the seismic stations recorded events between 2013 and 2018, and we further refine the number of stations used for analysis based on the availability of high-quality splitting results, as discussed in the following sections.

Methods

The MFAST (Savage, Wessel, et al., 2010) software filters the earthquake time-series, calculates the signal-to-noise ratio (SNR), and finally calculates the SWS parameters, including δt and ϕ. The only manual step of this software is to pick the P and S arrival times, which, in our case, has been done routinely by seismic analysts at OGS over the past decade.

The MFAST tool uses a combination of the minimum energy and the eigenvalue techniques developed by Silver and Chan (1991) and implements a cluster analysis on multiple measurement windows to determine the best results (Savage, Wessel, et al., 2010). The minimum energy method performs a grid search over all possible pairs of δt and ϕ and selects the pair that best removes the effects of splitting. The eigenvalue method will provide the best set of splitting parameters (ϕ and δt) when the smaller eigenvalue of the covariance matrix of two components is minimized. Multiple band-pass filters are used to find the best signal and frequency bands for parameter calculations. A broader band-pass filter is preferred over a narrow band-pass filter because the latter may cause cycle-skipping problems (Savage, Wessel, et al., 2010). For each event, the optimal band-pass filter is determined from a set of 14 predefined band-pass filters (Table S1, available in the supplemental material to this article) based on SNR and the width of the filter.

The SNR is calculated for the filtered data using the same window length (~3 s) for the signal and noise. The signal window starts immediately after the S-wave arrival (0.05–3.05 s), and the noise window precedes the S-wave arrival and includes an offset (−3.05 to −0.05 s) to account for possible inaccuracies in the S-wave arrival time (Savage, Wessel, et al., 2010). Furthermore, the noise window is chosen so as to include signal-generated noise during the P coda. The ratios of the root mean square between the signal amplitude and the noise amplitude from the north and east components are averaged to calculate the SNR (Savage, Wessel, et al., 2010). Measurements that are below the predefined minimum SNR (SNR < SNR$_{max}$, usually equals 3) are not considered at the time of interpretation. If more than one filter gives the same SNR value, the

Figure 1. Oklahoma map displaying the seismic sequence distribution (gray dots) between 2010 and 2019, fault systems (gray lines), seismic stations that recorded any seismic data between 2010 and 2019 (empty-black triangles), and seismic stations that fulfilled the quality-control parameters (filled-black triangles). The interest areas are as follows: (1) Kansas: stations KAN01 and KAN10 (orange); (2) Fairview: stations FW03 and OK039 (green); (3) Pawnee: stations PW11 and PW14 (yellow); (4) central Oklahoma: stations FNO and SMO (cyan). The color version of this figure is available only in the electronic edition.

measurement that is most stable with frequency is automatically chosen as the final measurement.

The minimum energy method can only be successfully applied when the polarization of the incoming waves is known (*SKS* and *SKKS* waves). On the other hand, the eigenvalue method can be used when the polarization is unknown, but this technique is very susceptible to noise, so it may provide less accurate splitting parameters in comparison with other splitting techniques that are less susceptible to noise such as the cross-correlation method (Fukao, 1984). Because the MFAST software uses both the minimum energy and the eigenvalue methods, depending on the type of data, the software should yield the best approximate solution for SWS parameters. For our case, in which we analyze local earthquakes, the eigenvalue method is used.

Results

We obtained 524,395 SWS measurements from the MFAST software. To ensure the reliability of subsequent analysis, we constrain the results by applying some quality-control factors. We follow previous studies (Savage, Wessel, *et al.*, 2010; Refayee *et al.*, 2014; Li and Peng, 2017; Cochran *et al.*, 2020) and define high-quality measurements by (1) A-grade parameters, which includes non-null measurements and an

SNR > 4; (2) delay time (δt) < 0.2 s because our sources are local seismicity; (3) fast direction error (f_err) < 10°; (4) delay time error (δt_err) < 0.05 s; and (5) epicentral distance (Δ) < 30 km to ensure that all sources are local events and that we have enough high-quality measurements per station. After applying these thresholds, we have 7916 high-quality measurements at 35 stations for local seismicity (epicentral distance (Δ) < 30 km). Cycle skipping, which may occur if the splitting program mismatches the predicted waveform data by an integer number of half-cycles away from the recorded waveform data (Savage, Wessel, *et al.*, 2010; Yao *et al.*, 2019), does not affect the splitting results due to the relatively short δt thresholding and the short event-station distances.

Short event-station distances may reduce the possibility of cycle skipping affecting results because the signals are not likely to experience significant scattering, attenuation, or dispersion over short distances. In addition, the splitting results do not qualitatively indicate being affected by cycle skipping because there is no clustering of δt. One hallmark of cycle skipping is anomalous clustering of splitting results in δt versus ϕ at δt half-periods (e.g., Matcham et al., 2000), which is not present in our results (Fig. S1). If MFAST utilizes distinctly different filter bands for splitting results at a particular station, inter-comparison of those splits at a single station may lead to the erroneous inference of ϕ nearly perpendicular to the correct value, as well as longer δt values (Robinson et al., 2020). Such a shift in ϕ and longer δt would be qualitatively similar to biased splitting results as could be produced by cycle skipping. We examined the filters that MFAST automatically chose and found that the filters were mostly common across all of the stations, as well as common within individual station results, and were generally the same three filters (Fig. S2).

Finally, we examined the splitting results to determine whether there was any systematic bias that could be introduced by regional lateral heterogeneity within the geologic structures. We scrutinized the splitting results (ϕ and δt) from various event azimuths. Figure S3 shows that there is not a systematic clustering of points when comparing azimuth with ϕ measurements. Similarly, Figure S4 shows that δt values do not exhibit any clustering for a specific range of event azimuths. These qualitative observations suggest that the thresholds that we set preclude any broad systematic biases from our splitting dataset. Finally, we plotted the results with different colors corresponding to similar filter groups for the automatically chosen filters. The lack of clustering in those observations suggests that the automatic software filter choice is not biasing the splitting results.

We show all stations that have more than 100 high-quality measurements in Oklahoma and southern Kansas in Figure 1. To illustrate subregional variations and the influence of data quality control, especially the effect of epicentral distance control, we present the SWS-determined ϕ for local seismicity (Fig. 2) for individual stations, and Figure 3 shows the overall behaviors from all measurements in each region. Figure S5 shows the relationship between δt and epicentral distance. We isolate eight representative stations in four distinct regions of the study area for detailed analysis: (1) southern Kansas: KAN01 and KAN10; (2) Fairview area, located in northwestern Oklahoma: FW06 and OK039; (3) Pawnee area, located in northeastern Oklahoma: PW11 and PW14; and (4) central Oklahoma: FNO and SMO.

In the following sections, we first perform statistical analyses of ϕ, then we discuss the spatial variations of ϕ in each region for local seismicity, and finally we discuss temporal variations of ϕ to examine if there are significant variations with time relating to pore pressure changes in the study region (Nolte et al., 2017).
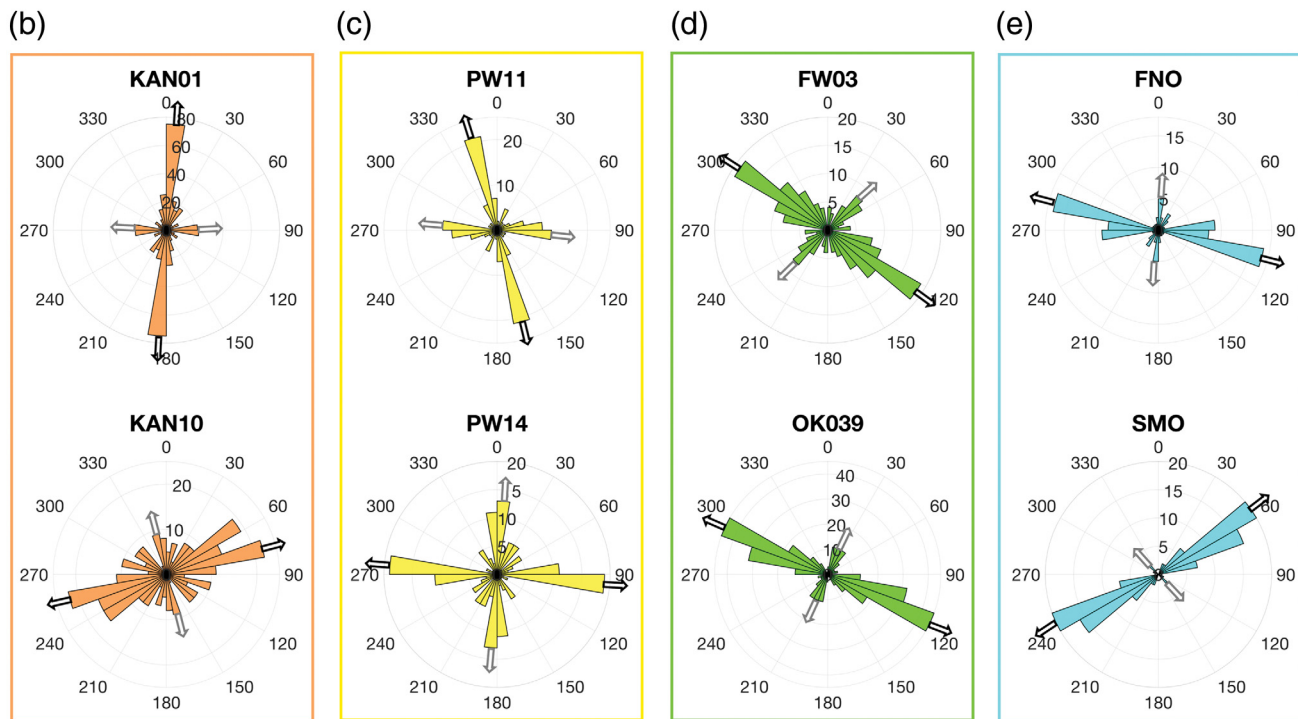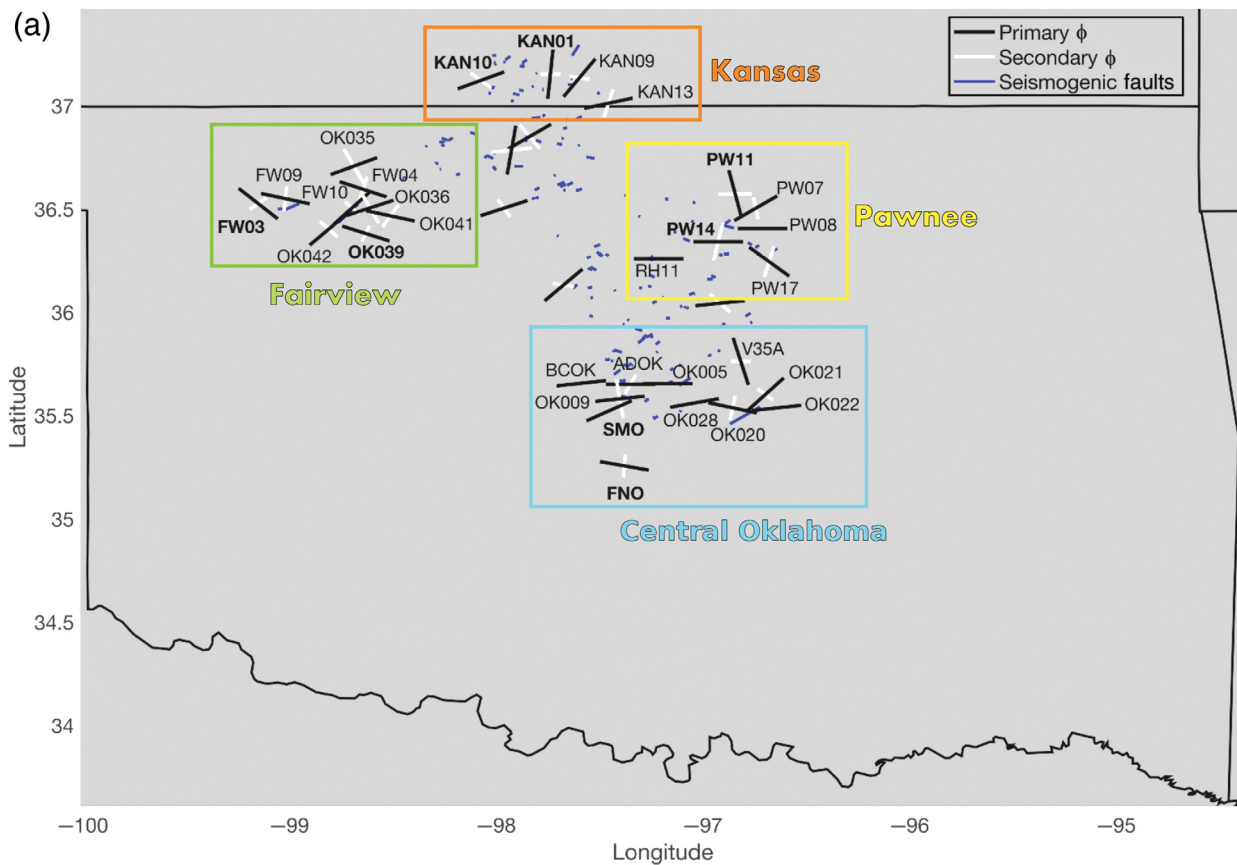
Primary and secondary fast directions

A polar histogram of the high-quality ϕ for each of the representative stations (Fig. 2) and each of the four regions (Fig. 3) suggests a peculiar characteristic that two predominant directions of ϕ are often observed (Figs. 2 and 3; note that a single value of ϕ is measured for each event station pair), a finding consistent with SWS analysis near the Prague, Oklahoma, area (Cochran et al., 2020). During field mapping of tensile fractures and small faults in the Precambrian basement exposure in southern Oklahoma, Kolawole et al. (2019) found two predominant trends of fractures and small-scale faults (northwest–southeast and northeast–southwest). This finding of two predominant trends is generally consistent with our results.

When primary (ϕ_{pri}) and secondary (ϕ_{sec}) fast polarization directions are observed at each station, we find the local maxima (peaks) among the SWS-measured histograms. We use the MATLAB (see Data and Resources) function findpeaks, which returns a vector with the local maxima (larger data sample) of the input histogram and their indices (peak locations) (MathWorks, 2020). ϕ_{pri} is defined as the most prominent peak, and ϕ_{sec} is defined as the second most prominent peak that is also found at least 30° away from the primary peak.

The relative strength of ϕ_{sec} is quantified based on the ratio between the number of measurements of ϕ_{sec} with respect to the number of measurements of ϕ_{pri}. We assign a threshold ratio of 0.25 to determine when there are enough secondary peak observations to designate the station as having a sufficiently significant secondary peak. As shown in Table S2 (SWS results), although we assigned secondary peaks for all 35 stations, only 28 stations exceeded the assigned threshold. In subsequent figures, we only plot the secondary ϕ_{sec} if it exceeds the threshold. Both ϕ_{pri} and ϕ_{sec} will be compared with the average regional $\sigma_{H\max}$ orientations (Qin et al., 2019) and fault orientations for both seismogenic faults (Qin et al., 2019) and mapped faults from the OGS database (Marsh and Holland, 2016), as well as mapped fractures in Kolawole et al. (2019) to better understand the potential dominant influencing factors for shear-wave anisotropy in the study region.

Spatial patterns of SWS from local seismicity (epicentral distance $\Delta < 30$ km)

Based on the results from local seismicity (Fig. 2), ϕ_{pri} and ϕ_{sec} are mostly quasi-perpendicular (almost perpendicular) to each other at most stations. The absolute difference in orientation between ϕ_{pri} and ϕ_{sec} for all stations ranges between 48° and 90° with a median difference of 78°, an absolute mean difference of 75.3°, and a mode of 72°. Because not all stations show a perfect orthogonal behavior, some stations can present an absolute difference in orientation greater than 90°. At stations FNO, GORE, OK009, OK020, OK022, and PW17, ϕ_{pri} and ϕ_{sec} are perpendicular to each other. We will discuss the spatial patterns for each of the four regions separately (Figs. 2 and 3).

Figure 2. (a) Regional map of Oklahoma and southern Kansas seismic network showing primary (black line: fixed length) and secondary (white line: length relative to $N_{\phi \sec}/N_{\phi \text{pri}}$) ϕ directions at each station from local seismicity (epicentral distance (Δ) < 30 km) and seismogenic faults from Qin *et al.* (2019) (blue lines). Polar histograms for the six isolated stations. (b) Kansas (orange): KAN01 (ϕ_{pri} : 6°; $\phi_{\sec}$: −90°) and KAN10 (ϕ_{pri} : 70°; $\phi_{\sec}$: −54°). (c) Pawnee (yellow): PW11 (ϕ_{pri} : −15°; $\phi_{\sec}$: 89°) and PW14 (ϕ_{pri} : 90°; $\phi_{\sec}$: 14°). (d) Fairview (green): FW03 (ϕ_{pri} : −52°; $\phi_{\sec}$: 55°) and OK039 (ϕ_{pri} : −72°; $\phi_{\sec}$: 26°). (e) Central Oklahoma (cyan): FNO (ϕ_{pri} : −80°; $\phi_{\sec}$: 5°) and SMO (ϕ_{pri} : 66°; $\phi_{\sec}$: −44°). The color version of this figure is available only in the electronic edition.
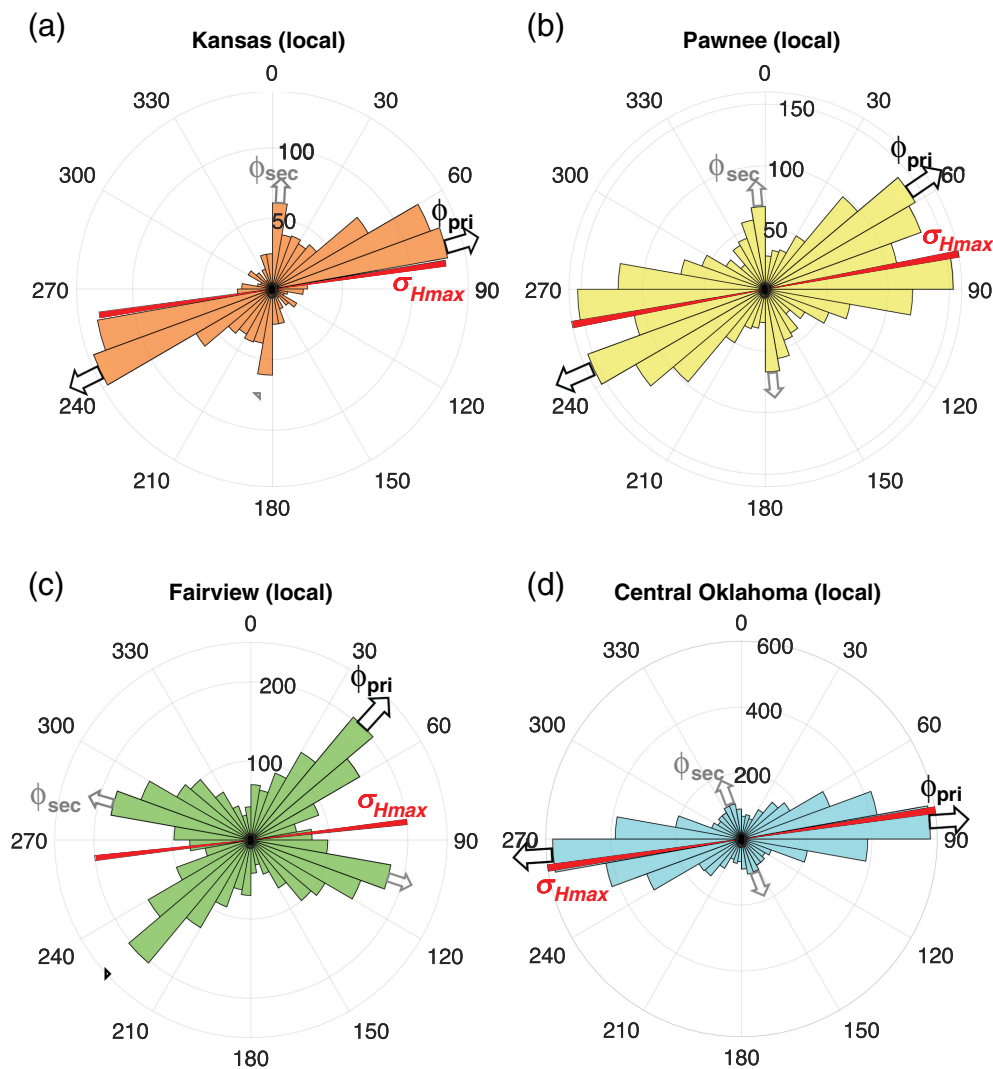
Figure 3. Statistical analysis of fast polarization directions from local seismicity results (includes all quality splits of the stations within the boxes on Fig. 2) and comparison with average regional $\sigma_{H\max}$ orientations (Qin *et al.*, 2019). (a) Southern Kansas, (b) Pawnee, (c) Fairview, and (d) central Oklahoma. The color version of this figure is available only in the electronic edition.
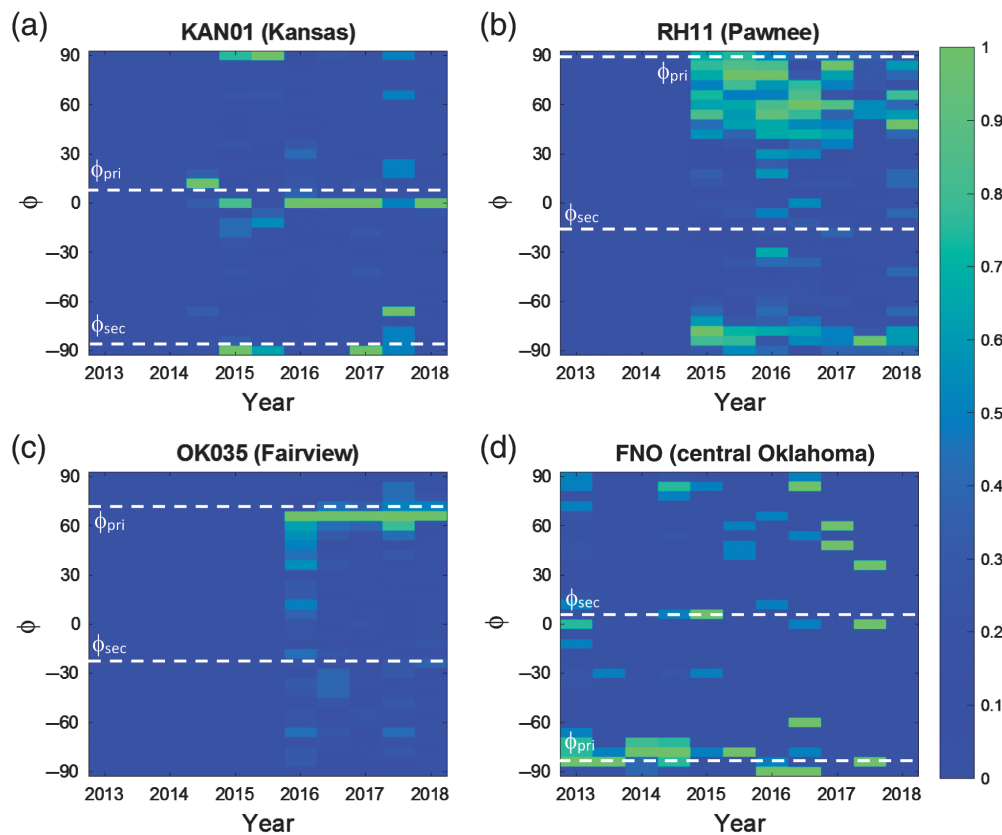
stations ϕ_{pri} shows a preferred east-northeast–west-southwest orientation, except station PW17, which shows a preferred west-northwest–south-southeast ϕ_{pri} orientation, and station PW11, which shows a preferred north–south ϕ_{pri} orientation (Fig. 2a). ϕ_{sec} does not show a general trend in the area, but ϕ_{pri} and ϕ_{sec} are perpendicular (PW17) or quasi-perpendicular to each other for most stations. The polar histograms of the representative stations (PW11 and PW14) clearly show such behavior (Fig. 2c).

Different from the previous two areas, Figure 3c indicates that the Fairview area shows an overall ϕ_{pri} at about 45° that deviates from the regional $\sigma_{H\max}$ orientation (Qin *et al.*, 2019) and a strong ϕ_{sec} that is about 65° away from the regional ϕ_{pri}. Figure 2d displays this relationship in the polar histograms of the representative stations (FW03 and OK039). Among all of the stations, ϕ_{pri} is aligned with one of the two dominate ϕ directions in Figure 3c: (1) the representative stations (FW03 and OK039) and stations FW04, FW09, and OK041 show a preferred ϕ_{pri} with a northwest–southeast orientation and a ϕ_{sec} in the northeast–southwest direction, except for station FW09, which shows a preferred ϕ_{sec} with a north–south orientation; (2) stations FW10, OK035, OK036, and OK042 show a dominant ϕ_{pri} with a northeast–southwest orientation and a ϕ_{sec} in the northwest–southeast direction.

Finally, in central Oklahoma, Figure 3d shows a ϕ_{pri} that is predominantly oriented east–west and well aligned with the regional $\sigma_{H\max}$ orientation (Qin *et al.*, 2019). ϕ_{sec} is weak and oriented in the north–south direction. This pattern is consistent with most individual stations in this region. The representative stations show perpendicular (FNO) and quasi-perpendicular (SMO) behavior between ϕ_{pri} and ϕ_{sec} (Fig. 2e). Stations SMO, OK021, OK022, and OK028 show a preferred northeast–southwest ϕ_{pri} orientation and a preferred

In southern Kansas, Figure 3a generally shows a strong overall ϕ_{pri} at about 75°, which is closely aligned with the regional $\sigma_{H\max}$ orientation (Qin *et al.*, 2019), and a weak regional ϕ_{sec}. However, ϕ_{pri} at stations in this region is variable: stations KAN10 and KAN13 show a ϕ_{pri} in the northeast–southwest direction, and at stations KAN01 and KAN09 ϕ_{pri} is oriented north–south. The overall ϕ_{pri} orientations are consistent with the ϕ analyzed in Nolte *et al.* (2017), especially those obtained from the Nanometrics Research Network (NX) and the U.S. Geological Survey Network (GS).

In the Pawnee area, Figure 3b shows a strong overall ϕ_{pri} ranging from 60° to 90°, also aligned with the regional $\sigma_{H\max}$ orientation (Qin *et al.*, 2019) and a weak regional ϕ_{sec}. However, individual stations show a more complex pattern. ϕ can still be grouped spatially, in which at the majority of

Figure 4. Fast polarization directions over time. 2D histograms for four of the isolated stations: (a) KAN01, (b) RH11, (c) OK035, and (d) FNO. On the vertical axis, the data are divided into 30 bins, with each bin being 6° long. On the horizontal axis, the data are divided into 12 bins, with each bin being 0.5 yr long. The color version of this figure is available only in the electronic edition.
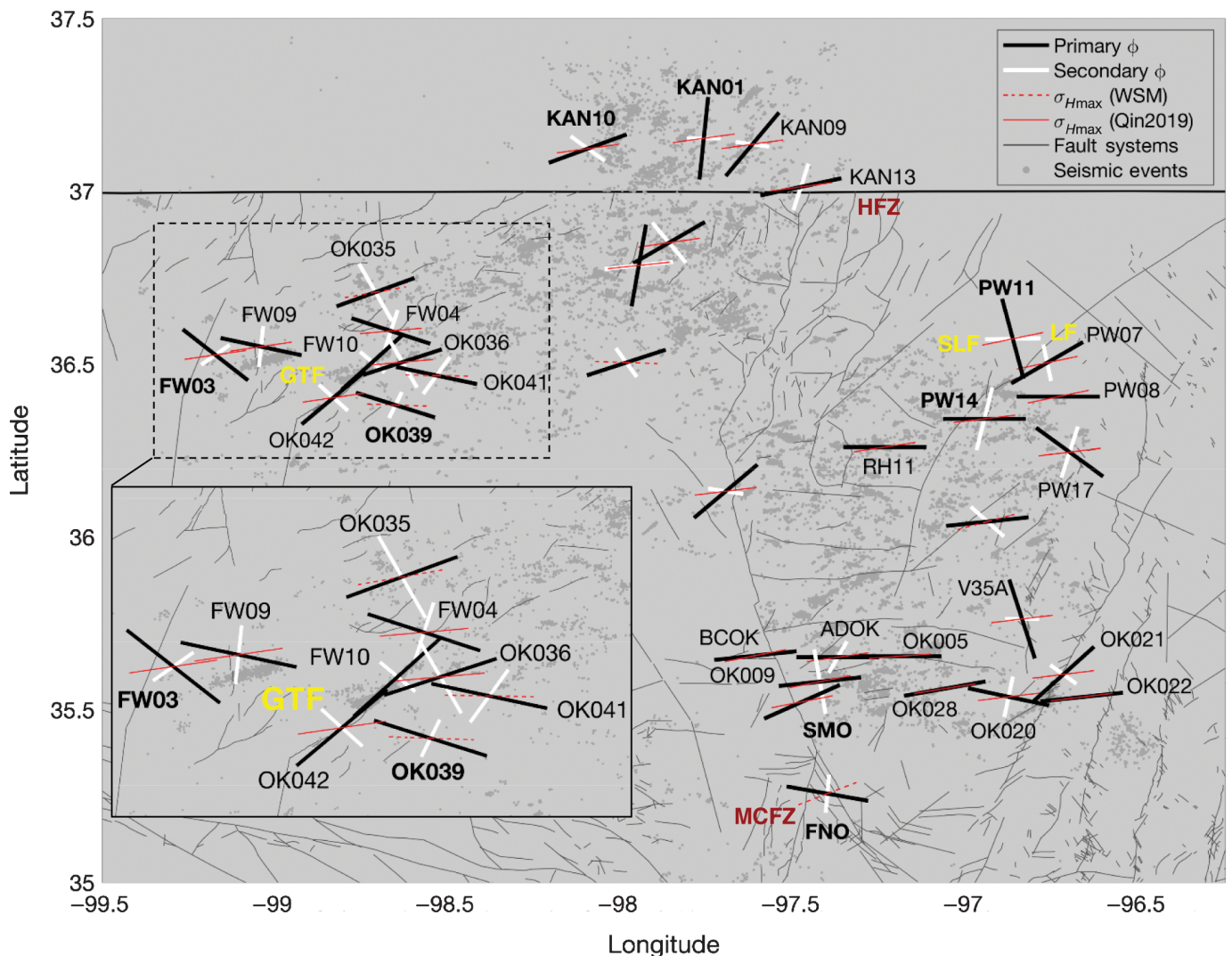
The temporal analysis at the four isolated stations (Fig. 4a–d) shows that ϕ values are mostly stable over time: (1) station KAN01 (Fig. 4a) shows that ϕ_{pri} is stable around 0° and ϕ_{sec} around −90° with some minor fluctuations in 2014 and at the end of 2018 for ϕ_{pri} and ϕ_{sec}. (2) Station RH11 (Fig. 4b) shows that ϕ_{pri} is mostly stable around 90° with some minor fluctuations of ±10°. (3) Station OK035 (Fig. 4c) shows that ϕ_{pri} and ϕ_{sec} are mostly stable around 72° and −30°, respectively. There are minor fluctuations of ±5° at the end of 2015 and beginning of 2016 for ϕ_{pri} and ϕ_{sec}. (4) Station FNO (Fig. 4d) shows that ϕ_{pri} is mostly stable around −90° and ϕ_{sec} around 0°, with some minor fluctuations over the study period.

Overall, Figure 4 and Figure S6 suggest that there is no variation in the fast polarization over time between 2013 and 2018, which is in contrast to a recent study (Nolte *et al.*, 2017) that identified subtle fluctuations of fast polarization directions (ϕ) over time between 2010 and 2015 in southern Kansas and northern Oklahoma.

northwest–southeast ϕ_{sec} orientation. Station V35A shows a peculiar behavior for this region by denoting a preferred ϕ_{pri} with a northwest–southeast orientation and ϕ_{sec} in the east–west direction, which is opposite to other stations in the region.

Temporal patterns of SWS

The spatial distribution of the stations with robust splitting results provides adequate coverage to identify temporally varying patterns of anisotropy in the study area. Because we applied quality-control thresholds to the results, we evaluate any variation over a 5 yr period (2013–2018). In Figure 4, we observe the distribution of the fast polarization directions over time for four stations, one station from each region (KAN01, RH11, OK035, and FNO). The data are plotted as 2D histograms. On the vertical axis, the data are divided into 30 bins, with each bin being 6°. On the horizontal axis, the data are divided into 12 bins, with each bin being 0.5 yr. These bins are shorter time windows than the several-year windows analyzed in Nolte *et al.* (2017). Within the temporal domain, each bin was normalized by dividing by the maximum number of measurements within each horizontal bin to highlight the highest density of fast direction measurements along the vertical axis.

Discussion

Our SWS results from 9 yr of data (2010–2019) provide a robust SWS parameters dataset for 35 stations in Oklahoma and southern Kansas (Table S2). The presence of both primary (ϕ_{pri}) and secondary (ϕ_{sec}) fast directions of polarizations indicates that fast polarization directions (ϕ) in the U.S. midcontinent are sensitive to maximum horizontal stresses in the area and possibly also are sensitive to other large-scale local structures (e.g., fault and fracture systems) or microstructural elements in the granitic basement. Analyses of spatial patterns show that three out of the four study regions show consistency between regional overall primary (ϕ_{pri}) and regional average $\sigma_{H\,max}$ orientation (Qin *et al.*, 2019), which are generally consistent with those presented in Cochran *et al.* (2020), in which the orientation of ϕ_{pri} corresponds to previously calculated horizontal stress orientations. Basement structures throughout central Oklahoma consist of faulted basement blocks and interconnected mafic sills (Kolawole *et al.*, 2020), and these

Figure 5. Regional comparison between primary ϕ (black line: fixed length), secondary ϕ (white line: length relative to $N_{\phi\,\text{sec}}/N_{\phi\text{pri}}$), and $\sigma_{H\,\text{max}}$ orientations (red) from local seismicity results (epicentral distance $(\Delta) < 30$ km). Red-dashed line: World Stress Map (WSM) measurements. Red-solid line: Qin et al. (2019) measurements. Gray lines: Mapped faults in which features are referred to in the Introduction and Primary and Secondary Fast Directions sections, including faults annotated with yellow text and fault zones annotated in dark red. GTF, Galena Township fault; HFZ, Humboldt fault zone; LF: Labette fault; MCFZ: McClain County fault zone; SLF, Sooner Lake fault. The color version of this figure is available only in the electronic edition.

structural features are inherited by overlying stratigraphy (Patel *et al.*, 2020). The splitting results are sensitive to these features. The presence of ϕ_{sec} is plausibly influenced by local stress anomalies or other secondary geologic structures. Cochran *et al.* (2020) suggest that secondary polarization may indicate the presence of shear fabric aligned subparallel to main faults in the region.

In the Fairview region, we observe two strong peaks in overall fast polarization directions, in which ϕ_{pri} is aligned with the regional average $\sigma_{H\,\text{max}}$ orientation at some stations, and the major fault in this region is not optimally oriented for slip within the current regional stress field (Qin *et al.*, 2019).

To better understand the factors that influence SWS parameters, we examine the detailed relationship among fast polarization directions at each station (including primary (ϕ_{pri}) and secondary (ϕ_{sec})), $\sigma_{H\,\text{max}}$ orientation at each station (from Qin *et al.*, 2019, or the World Stress Map [WSM]; Heidbach *et al.*, 2016, 2018), and fault maps in each region (seismogenic faults from Qin *et al.*, 2019 and sedimentary faults from Marsh and Holland, 2016). This information is displayed in Figures 2a and 5.

In southern Kansas, there is not a clear general correspondence between ϕ_{pri} and $\sigma_{H\,\text{max}}$ orientations at all of the stations (Fig. 5). At station KAN13, ϕ_{pri} and $\sigma_{H\,\text{max}}$ show a direct correlation, and at station KAN10, ϕ_{pri} and $\sigma_{H\,\text{max}}$ are similarly oriented, but the correlation is not as strong. However, at stations KAN01 and KAN09, ϕ_{pri} values are in alignment with the orientation of the Humboldt fault zone (HFZ), which is one of the most seismically active areas in Kansas, particularly

where the HFZ is intersected by cross-cutting structures (Luza et al., 1982). There is good correspondence between ϕ_{sec} and the seismogenic faults (faults capable of generating earthquakes) in this area (Fig. 2a or refer to fig. 7 of Qin et al., 2019). However, apart from the HFZ and the seismogenic faults in this region, it is unclear what faults and other structures directly underlie the area where the Kansas stations are located. Local statistical analysis of ϕ (Fig. 3a) suggests that ϕ_{pri} is largely consistent with maximum horizontal stresses and ϕ_{sec} is consistent with subsurface structures and crustal heterogeneities.

In Pawnee (Fig. 5), there is good correspondence among ϕ_{pri}, $\sigma_{H\max}$, and seismogenic faults (Qin et al., 2019) (e.g., the Sooner Lake fault [SLF] that hosted the **M** 5.8 Pawnee earthquake; Chen et al., 2017) at multiple stations. From Figure 3, we can suggest that fast polarization directions in this region are mostly influenced by horizontal stresses in the area. The presence of ϕ_{sec} is probably caused by local stress perturbations or local fault structures (e.g., the SLF and the Labette fault).

In Fairview, most of the stations show obliqueness between the fault systems in this region and ϕ_{pri}, specifically with the Galena Township Fault (GTF) that hosted the **M** 5 Fairview earthquake (Goebel et al., 2017). At stations OK036, OK039, and OK041, there is good correspondence among ϕ_{pri}, $\sigma_{H\max}$, mapped faults, and otherwise unmapped faults delineated by seismicity lineaments (Qin et al., 2019) (Fig. 5). However, stations OK035 and FW09 show a close resemblance between ϕ_{pri} and $\sigma_{H\max}$ (Fig. 5). Statistical analysis of fast polarization directions (Figs. 2a and 3c) suggests that seismogenic and sedimentary faults may be a more dominant factor in controlling crustal anisotropy, rather than horizontal stress, in this area. Qin et al. (2019) also identified some oblique normal faulting from focal mechanism analysis, and stress inversions suggest the presence of a transtensional stress field in the Fairview area compared with a predominantly strike-slip stress field in most of the rest of central Oklahoma.

Central Oklahoma shows the best correlation between ϕ_{pri} and $\sigma_{H\max}$ (Fig. 5). In addition, some of these fast polarization directions (ϕ) are parallel to the fault systems in this area. Stations in the southeast corner of this region are not bounded by fault systems or significant geological structures. On the contrary, ϕ_{sec} is parallel to the McClain County fault zone at station FNO. From Figure 3 and the excellent correspondence between ϕ_{pri} and $\sigma_{H\max}$ in Figure 5, we can suggest that horizontal stresses are likely the driving factor of fast polarization direction in the area.

These comparisons suggest that the stress field and seismogenic and sedimentary faults are major factors that influence crustal anisotropy in the four study regions, although the dominant control factors may vary by region. Temporal stability of fast directions suggests that tectonic stresses have been stable for the duration of this study and that the influence of pore pressure changes on crustal anisotropy is relatively small if it occurs or it may not be measurable at the scale of our study. If our results are common to other regions, it suggests that SWS results are sensitive to both pre-existing structures and alignment with $\sigma_{H\max}$. Thus, prior to planned oil and gas activities, SWS could inform the reactivation potential of pre-existing faults without requiring detailed prior knowledge or mapping of those systems, assuming that $\sigma_{H\max}$ is known.

Conclusion

A regional SWS analysis was performed to identify spatial patterns of anisotropy in the central United States over 9 yr (2010–2019). We obtained 7916 high-quality SWS parameters from local seismicity at 35 stations in Oklahoma and southern Kansas. We present an SWS dataset (Table S2) that is fully reproducible due to the implementation of completely automated methodologies. We observe that almost all stations show the presence of a preferred primary fast direction of polarization (ϕ_{pri}) and a secondary fast direction of polarization (ϕ_{sec}). At most stations in Oklahoma, ϕ_{pri} correlates with the orientation of horizontal stresses in the region ($\sigma_{H\max}$) obtained from focal mechanism inversions (Qin et al., 2019) and WSM measurements (Heidbach et al., 2016, 2018). However, some stations show small deviations between ϕ_{pri} and $\sigma_{H\max}$ orientations, especially in the Fairview region, where at most stations neither ϕ_{pri} nor ϕ_{sec} values are in good alignment with $\sigma_{H\max}$. These discrepancies are potentially caused by local structures in the area (e.g., fault networks). ϕ_{sec} is potentially caused by local stress perturbations in the area. An expanded SWS catalog across the central United States could be an important tool for better understanding the regional variations of the orientation of maximum horizontal stress and major fault networks.

Data and Resources

Declaration of Competing Interests

Acknowledgments

References

Alt, R. C., and M. D. Zoback (2017). In situ stress and active faulting in Oklahoma, *Bull. Seismol. Soc. Am.* **107,** no. 1, 216–228, doi: 10.1785/0120160156.

Baird, A. F., J. M. Kendall, J. P. Verdon, A. Wuestefeld, T. E. Noble, Y. Li, M. Dutko, and Q. J. Fisher (2013). Monitoring increases in fracture connectivity during hydraulic stimulations from temporal variations in shear wave splitting polarization, *Geophys. J. Int.* **195,** no. 2, 1120–1131, doi: 10.1093/gji/ggt274.

Chen, X., N. Nakata, C. Pennington, J. Haffener, J. C. Chang, X. He, Z. Zhan, S. Ni, and J. I. Walter (2017). The Pawnee earthquake as a result of the interplay among injection, faults and foreshocks, *Sci. Rep.* **7,** no. 4945, 1–18, doi: 10.1038/s41598-017-04992-z.

Cochran, E. S., R. J. Skoumal, D. McPhillips, Z. E. Ross, and K. M. Keranen (2020). Activation of optimally and unfavorably oriented faults in a uniform local stress field during the 2011 Prague, Oklahoma, sequence, *Geophys. J. Int.* doi: 10.1093/gji/ggaa153.

Crampin, S. (1984). Effective anisotropic elastic constants for wave propagation through cracked solids, *Geophys. J. Roy. Astron. Soc.* **76,** no. 1, 135–145, doi: 10.1111/j.1365-246X.1984.tb05029.x.

Darold, A. P., A. A. Holland, K. Jennifer, and A. R. Gibson (2015). Oklahoma earthquake summary report 2014, *Oklahoma Geol. Surv. Open-File Rept. OF1-2015*.

Denison, R. E., E. G. Lidiak, M. E. Bicford, and E. B. Kisvarsanyi (1984). Geology and geochronology of Precambrian rocks in the central interior region of the United States, *U.S. Geol. Surv. Profess. Pap. 1241-C*, 1–13.

Ellsworth, W. L. (2013). Injection-Induced Earthquakes, *Science* **341,** no. 6142, 142, doi: 10.1126/science.1225942.

Fukao, Y. (1984). Evidence from core-reflected shear waves for anisotropy in the Earth's mantle, *Nature* **309,** no. 5970, 695–698, doi: 10.1038/309695a0.

Gao, Y., J. Wu, Y. Fukao, Y. Shi, and A. Zhu (2011). Shear wave splitting in the crust in North China: Stress, faults and tectonic implications, *Geophys. J. Int.* **187,** no. 2, 642–654, doi: 10.1111/j.1365-246X.2011.05200.x.

Goebel, T., M. Weingarten, X. Chen, J. Haffener, and E. E. Brodsky (2017). The 2016 M_w 5.1 Fairview, Oklahoma earthquakes: Evidence for long-range poroelastic triggering at 40 km from fluid disposal wells, *Earth Planet. Sci. Lett.* **472,** 50–61, doi: 10.1016/j.epsl.2017.05.011.

Heidbach, O., M. Rajabi, X. Cui, K. Fuchs, B. Müller, J. Reinecker, K. Reiter, M. Tingay, F. Wenzel, F. Xie, *et al.* (2018). The World Stress Map database release 2016: Crustal stress pattern across scales, *Tectonophysics* **744,** 484–498, doi: 10.1016/j.tecto.2018.07.007.

Heidbach, O., M. Rajabi, K. Reiter, M. Ziegler, and , and World Stress Map Team (2016). *World Stress Map Database Release 2016*, GFZ Data Services, doi: 10.5880/WSM.2016.001.

Holland,, A. (2013). Earthquakes triggered b hydraulic fracturing in south-central Oklahoma, *Bull. Seismol. Soc. Am.* **103,** no. 3, 1784–1792, doi: 10.1785/0120120109.

Johnson, J. H., and M. K. Savage (2012). Tracking volcanic and geothermal activity in the Tongariro Volcanic Centre, New Zealand, with shear wave splitting tomography, *J. Volcanol. Geoth. Res.* **223–224,** 1–10, doi: 10.1016/j.jvolgeores.2012.01.017.

Kolawole, F., C. S. Johnston, C. B. Morgan, J. C. Chang, K. J. Marfurt, D. A. Lockner, Z. Reches, and B. M. Carpenter (2019). The susceptibility of Oklahoma' basement to seismic reactivation, *Nature Geosci.* **12,** 839–844, doi: 10.1038/s41561-019-0440-5.

Kolawole, F., M. Simpson-Turko, and B. M. Carpenter (2020). Basement-controlled deformation of sedimentary sequences, Anadarko Shelf, Oklahoma, *Basin Res.* doi: 10.1111/bre.12433.

Li, Z., and Z. Peng (2017). Stress- and structure-induced anisotropy in southern California from two decades of shear wave splitting measurements, *Geophys. Res. Lett.* **44,** no. 19, 9607–9614, doi: 10.1002/2017GL075163.

Luza, K. V., J. E. Lawson, C. Barrett, N. F. Rasmussen, D. J. Santiago, and R. C. Shoup (1982). *Seismicity and Tectonic Relationships of the Nemaha Uplift in Oklahoma. Part IV / Prepared by Kenneth V. Luza, James E. Lawson, Jr. ; with Contributions by Christopher Barrett ... [et al.]; Prepared for Division of Reactor Safety Research, Office of Nuclear Regulatory Research, U.S. Nuclear Regulatory Commission Under Contract No. NRC 04-76-314*, Special publication (Oklahoma Geological Survey); 82-1, Oklahoma Geological Survey, Norman, Oklahoma, 52 pp.

Marsh, S., and A. Holland (2016). Comprehensive fault database and interpretative fault map of Oklahoma, *Geol. Surv. Open-File Rept. OF2-2016*, Oklahoma Geological Survey, Norman, Oklahoma, 15 pp.

Matcham, I., M. K. Savage, and K. R. Gledhill (2000). Distribution of seismic anisotropy in the subduction zone beneath the Wellington region, New Zealand, *Geophys. J. Int.* **140,** no. 1, 1–10.

MathWorks (2020). Findpeaks, signal processing toolbox documentation, The MathWorks, Inc., available at https://www.mathworks.com/help/signal/ref/findpeaks.html#buhdm28-1 (last accessed March 2021).

Nolte, K. A., G. P. Tsoflias, T. S. Bidgoli, and W. L. Watney (2017). Shear-wave anisotropy reveals pore fluid pressure-induced seismicity in the U.S. midcontinent, *Sci. Adv.* **3,** no. 12, 1–7, doi: 10.1126/sciadv.1700443.

Patel, S., F. J. I. Kolawole Walter, X. Chen, and K. J. Marfurt (2020). Seismic illumination of small-offset seismogenic faults, Anadarko basin, Oklahoma, *Interpretation* **9,** no. 2, 1–50.

Qin, Y., X. Chen, J. I. Walter, J. Haffener, D. T. Trugman, B. M. Carpenter, M. Weingarten, and F. Kolawole (2019). Deciphering the stress state of seismogenic faults in Oklahoma and southern Kansas based on an improved stress map, *J. Geophys. Res.* **124,** no. 12, 12,920–12,934, doi: 10.1029/2019JB018377.

Refayee, H. A., B. B. Yang, K. H. Liu, and S. S. Gao (2014). Mantle flow and lithosphere–asthenosphere coupling beneath the southwestern edge of the North American craton: Constraints from shear-wave splitting measurements, *Earth Planet. Sci. Lett.* **402,** 209–220, doi: 10.1016/j.epsl.2013.01.031.

Robinson, I., S. Robinson, and D. Robinson (2020). Novel infrasound monitor project: Real geophysics research on a budget, *Phys. Educ.* **55,** 055025, doi: 10.1088/1361-6552/ab9e9d.

Savage, M. K., T. Ohminato, Y. Aoki, H. Tsuji, and S. M. Greve (2010). Stress magnitude and its temporal variation at Mt. Asama Volcano, Japan, from seismic anisotropy and GPS, *Earth Planet. Sci. Lett.* **290,** nos. 3/4, 403–414, doi: 10.1016/j.epsl.2009.12.037.

Savage, M. K., A. Wessel, N. A. Teanby, and A. W. Hurst (2010). Automatic measurement of shear wave splitting and applications to time varying anisotropy at Mount Ruapehu volcano, New Zealand, *J. Geophys. Res.* **115,** no. 12, 1–17, doi: 10.1029/2010JB007722.

Schoenball, M., and W. L. Ellsworth (2017a). A systematic assessment of the spatio-temporal evolution of fault activation through induced seismicity in Oklahoma and southern Kansas, *J. Geophys. Res.* **122,** 10,189–10,206, doi: 10.1002/2017JB014850.

Schoenball, M., and W. L. Ellsworth (2017b). Waveform-relocated earthquake catalog for Oklahoma and southern Kansas illuminates the regional fault network, *Seismol. Res. Lett.* **88,** no. 5, 1252–1258, doi: 10.1785/0220170083.

Silver, P., and W. Chan (1991). Shear wave splitting and subcontinental mantle deformation, *J. Geophys. Res.* **96,** no. 10, 16,429–16,454, doi: 10.1029/91JB00899.

Skoumal, R. J., J. Ole Kaven, and J. I. Walter (2019). Characterizing seismogenic fault structures in Oklahoma using relocated template-matched catalog, *Seismol. Res. Lett.* **90,** no. 4, 1535–1543, doi: 10.1785/0220190045.

Tadokoro, K., and M. Ando (2002). Evidence for rapid fault healing derived from temporal changes in S wave splitting, *Geophys. Res. Lett.* **29,** no. 4, 6-1–6-4, doi: 10.1029/2001GL013644.

Unglert, K., M. K. Savage, N. Fournier, T. Ohkura, and Y. Abe (2011). Shear wave splitting, V_P/V_S, and GPS during a time of enhanced activity at Aso caldera, Kyushu, *J. Geophys. Res.* **116,** no. 11, 1–14, doi: 10.1029/2011JB008520.

Verdon, J. P., J. M. Kendall, and A. Wüstefeld (2009). Imaging fractures and sedimentary fabrics using shear wave splitting measurements made on passive seismic data, *Geophys. J. Int.* **179,** no. 2, 1245–1254, doi: 10.1111/j.1365-246X.2009.04347.x.

Walsh, F. R., and M. D. Zoback (2015). Oklahoma's recent earthquakes and saltwater disposal, *Sci. Adv.* **1,** 1–9, doi: 10.1126/sciadv.1500195.

Walter, J. I., P. Ogwari, A. Thiel, F. Ferrer, I. Woelfel, J. C. Chang, A. P. Darold, and A. A. Holland (2020). The Oklahoma Geological Survey statewide seismic network, *Seismol. Res. Lett.* **91,** no. 2A, 611–621, doi: 10.1785/0220190211.

Wuestefeld, A., J. M. Kendall, J. P. Verdon, and A. Van As (2011). In situ monitoring of rock fracturing using shear wave splitting analysis: An example from a mining setting, *Geophys. J. Int.* **187,** no. 2, 848–860, doi: 10.1111/j.1365-246X.2011.05171.x.

Yao, G., N. V. da Silva, M. Warner, D. Wu, and C. Yang (2019). Tackling cycle skipping in full-waveform inversion with intermediate data, *Geophysics* **84,** R411–R427, doi: 10.1190/geo2018-0096.1.